PAPER

Intrinsic pinning by naturally occurring correlated defects in $FeSe_{1-x}Te_x$ superconductors

To cite this article: M L Amigó *et al* 2017 *Supercond. Sci. Technol.* **30** 085010

IOP Publishing Superconductor Science and Technology
Supercond. Sci. Technol. 30 (2017) 085010 (11pp) https://doi.org/10.1088/1361-6668/aa757c

Intrinsic pinning by naturally occurring correlated defects in $FeSe_{1-x}Te_x$ superconductors

M L Amigó[1], M V Ale Crivillero[1], D G Franco[1,5], A Badía–Majós[2], J Guimpel[1], J Campo[2], F Damay[3], F Porcher[3], A M Condó[4] and G Nieva[1]

[1] Low Temperature Lab, Centro Atómico Bariloche (CNEA) and Instituto Balseiro, (U.N.Cuyo-CNEA) and CONICET, 8400-Bariloche, Río Negro, Argentina
[2] Dep. Física de la Materia Condensada–Inst. Ciencia de Materiales de Aragón, Universidad de Zaragoza–CSIC, E-50009 Zaragoza, Spain
[3] Laboratoire Léon Brillouin, CEA-CNRS UMR 12, F-91191 Gif sur Yvette Cedex, France
[4] Metal Physics Lab, Centro Atómico Bariloche (CNEA) and Instituto Balseiro, (U.N.Cuyo-CNEA) and CONICET, 8400-Bariloche, Río Negro, Argentina

E-mail: gnieva@cab.cnea.gov.ar

Received 9 March 2017, revised 19 May 2017
Accepted for publication 30 May 2017
Published 12 July 2017

Abstract

We study the angular dependence of dissipation in the superconducting state of FeSe and $Fe(Se_{1-x}Te_x)$ through electrical transport measurements, using crystalline intergrown materials. We reveal the key role of the inclusions of the non superconducting magnetic phase $Fe_{1-y}(Se_{1-x}Te_x)$, growing into the $Fe(Se_{1-x}Te_x)$ pure β-phase, in the development of a correlated defect structure. The matching of both atomic structures defines the growth habit of the crystalline material as well as the correlated planar defects orientation.

Keywords: Fe chalcogenides superconductors, electrical transport, crystalline phases intergrowth

(Some figures may appear in colour only in the online journal)

1. Introduction

Within the Fe-based superconductors, the PbO type Fe chalcogenides, i.e.: the '11' compounds, have the simplest structure but a very complex electronic and magnetic behavior [1]. In particular, the normal and superconducting states of $Fe(Se_{1-x}Te_x)$ are strongly influenced by hydrostatic and chemical pressure [2, 3]. Furthermore, due to the very rich thermodynamic phase diagram [4], slight differences in material synthesis yield a variation in composition and the appearance of defects that significantly change the electronic and magnetic properties. The emergence of the hexagonal and magnetic (NiAs type structure) Fe_7Se_8 intergrowth in the (PbO type tetragonal) β-FeSe matrix, has been the source of confusion in earlier reports of superconducting and normal properties of these materials. A low temperature synthesis is needed to grow clean single crystals of the tetragonal β phase of these compounds [5]. Despite the above, the intergrown samples are very useful for understanding the effect on normal state electronic properties of magnetic ordering within the non magnetic matrix, and also of the microscopic stress induced changes in the normal state properties and in the superconducting parameters in the mixed state. On the other hand, the microscopic geometry of the intergrown phases structural coupling determines the kind of defects (geometry and distribution) that influence the vortex dynamics in the dissipationless state and the properties of the dissipation below the superconducting critical field and above the zero critical current state. In a certain range of defect density, the potential application of these materials in wires or tapes, has to be considered. These intergrown crystals are possible emergent materials suitable for application given their high superconducting critical field and the simple way to generate correlated defects in them.

[5] Present address: Max-Planck-Institute for Chemical Physics of Solids, D-01187 Dresden, Germany.

This article is focused on the correlated defects in superconducting FeSe and in the $Fe(Se_{1-x}Te_x)$ family. We study the microscopic nature of these defects characterizing local and bulk transport properties. Correlation is established by combination of a number of microscopic and macroscopic experimental techniques in a wide range of applied temperatures and magnetic fields. This has allowed us to separate the intrinsic and defect induced contributions to superconductivity.

2. Crystal growth and characterization

$Fe_{1-y}(Se_{1-x}Te_x)$ crystals of nominal composition $x = 0$, 0.25, 0.5, 0.75 and 1 with an intergrowth of two phases were obtained by a multi-step method. The starting materials were >4N powders of Fe, Se and Te, ball milled in Ar atmosphere. The obtained $Fe(Se_{1-x}Te_x)$ powders were sealed in an evacuated quartz tube and fired at 680 °C for 48 h, in order to obtain a polycrystalline material. Low heating rates were used while the temperature was close to the melting point of Se and Te and the cooling rates were free in all cases. Afterwards, $Fe_{1-y}(Se_{1-x}Te_x)$ crystals were grown in evacuated double quartz ampoules using a 1/4 KCl:3/4 NaCl flux, and a molar proportion $Fe(Se_{1-x}Te_x)$:flux of 1:50. The upper temperature reached depended on the composition of the crystals, increasing with the Te content. For $x = 0$, 0.25, 0.5, 0.75 and 1 the final temperatures were 850 °C, 868 °C, 885 °C, 903 °C and 920 °C respectively. The cooling rates were 0.05 °C min^{-1} from the final temperature to 600 °C. At 400 °C the quartz tubes were quenched in water. Finally, the crystals were released dissolving the flux with water.

Platelet-like shaped crystals were obtained. As explained below, the microstructure was characterized by room temperature x-ray (XR) diffraction and transmission electron microscopy (TEM). Additional structural studies of the powders, so as to assess a number of physical parameters (characteristic structural and magnetic transition temperatures), were performed by neutron thermo-diffraction (see appendix for details). The crystal composition was measured by energy dispersive spectroscopy (EDS). Angle resolved transport measurements were performed with a conventional four-wire method in a superconducting magnet up to 16 T. For such investigation, the crystals were mounted onto a rotatable sample holder with an angular resolution of 0.05°. Magnetization and superconducting volume fraction of the samples were determined using a QD-SQUID magnetometer with a zero field cooling protocol.

The resulting crystalline samples show Fe deficiency as indicated by EDS. Samples without Te have an average composition of $Fe_{0.89}Se$, while crystals containing Te have a lower average Fe concentration: $(1-y) \simeq 0.78$. This is an indication that the crystals have a mixture of structural phases because pure β-phase with a tetragonal PbO type structure would be near $y = 0$. It is therefore expected to find inclusions of NiAs type hexagonal phase. Indeed, the XR diffraction data of our crystals show the presence of both tetragonal and hexagonal phases. Other authors have found nanoscaled hexagonal phase in a tetragonal matrix and that the shape and size of this

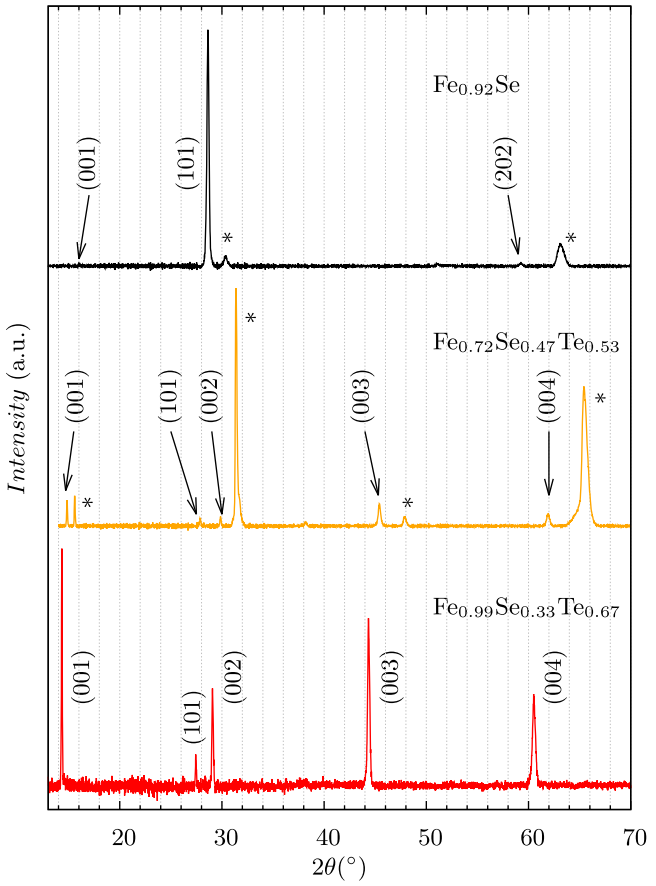

Figure 1. XR diffraction patterns for $Fe_{0.92}Se$, $Fe_{0.72}(Se_{0.47}Te_{0.53})$ and $Fe_{0.99}(Se_{0.33}Te_{0.67})$. Numbers in brackets indicate the Miller indices for the tetragonal phase. $*$ indicates peaks corresponding to the (00l) family of the hexagonal phase.

intergrowth depends on the crystal growth speed [6]. Figure 1 shows XR diffraction patterns for $Fe_{1-y}(Se_{1-x}Te_x)$ crystals, with the incidence plane of the XR perpendicular to the platelet's surface. We show results for samples with the lower and the higher Fe content.

For $Fe_{1-y}Se$, we identified the tetragonal PbO type structure with the space group P4/nmm of the β phase and the hexagonal NiAs type structure of the Fe_7Se_8 ($Fe_{0.875}Se$) compounds. In the tetragonal phase, we found the reflections from (00l) and (l0l) planes families, while in the hexagonal phase, only the (00l) reflections were present. For the samples containing Te, we observed that those with lower Fe content have larger hexagonal phase peaks and that the (l0l) reflections are comparatively less intense.

Figure 2 shows two different behaviors of the c axis parameter as a function of Te concentration, corresponding to the tetragonal and hexagonal phases. The c axis of the tetragonal phase increases with x, in good agreement with the measurements of other authors [7–11, 16]. On the other hand, the c axis of the hexagonal phase decreases with the content of Te. We also show in figure 2 that our hexagonal phase c axis data coincide with those taken by Terzief [15] who studied the structural properties of the solid solution $Fe_{1-y}(Se_{1-x}Te_x)$ between Fe_7Se_8 and Fe_2Te_3. It is worth

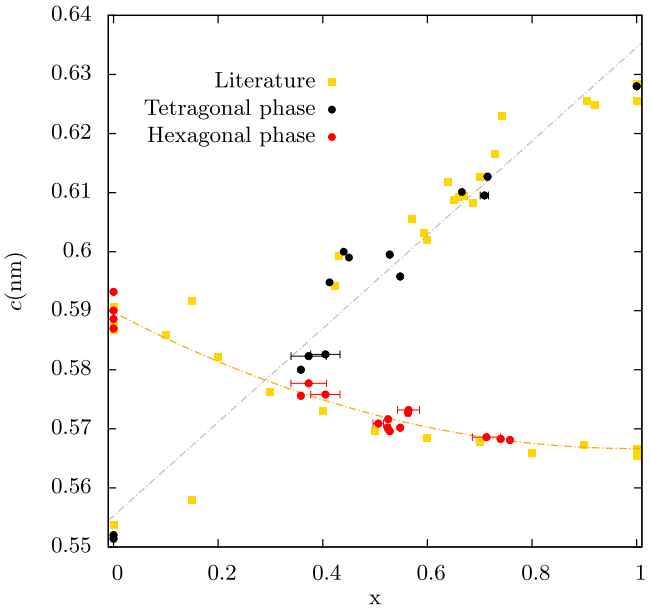

Figure 2. c lattice parameter of the tetragonal and hexagonal phases as a function of the content of Te. Square symbols show data from the literature [7–16].

mentioning that, in spite of the Te ions being bigger than the Se ones, the c axis decreases with increasing Te content. According to our observations, this is due to the increase in the amount of Fe vacancies and to the fact that the structural parameters of the hexagonal phase change smoothly and continuously from Fe_7Se_8 to Fe_2Te_3.

In the magnetization measurements it is expected to find characteristics of both phases present in our crystals. Figure 3 shows the temperature dependence of the magnetization with an applied magnetic field of 0.1 T perpendicular to the crystal plane for different Te concentrations. At low temperatures, there is a drop in the magnetization due to the superconducting transition. Due to the presence of the hexagonal phase, the behavior in the normal state depends on the Te concentration. As described in the literature [15], concomitant Fe vacancies are located in alternate planes and as long as they are ordered, the material is magnetic. Depending on the value of y, hexagonal $Fe_{1-y}Se$, is ferrimagnetic (FM), antiferromagnetic (AF) or has a transition from FM to AF [17]. Fe_7Se_8 has two types of vacancy superstructures called $3c$ and $4c$. They both have a FM behavior at high temperatures and at $\sim$130 or $\sim$220 K they have a change in the easy axis of magnetization causing a drop in the magnetization (AF) [18].

In figure 3, $Fe_{0.92}Se$ has a broad hump at $\sim$150 K that we associated with the presence of hexagonal phase, Fe_7Se_8 with vacancies superstructure, in agreement with our magnetic neutron diffraction study presented in the appendix.

With increasing Te content, the hump rapidly disappears as expected if the hexagonal phase content decreases. In the case of $Fe_{0.72}(Se_{0.47}Te_{0.53})$, the system tends to order at temperatures below 100 K but does not saturate. In the samples with more Te, the system is paramagnetic. In the inset of figure 3 the susceptibility as a function of temperature below the superconducting onset is shown for a

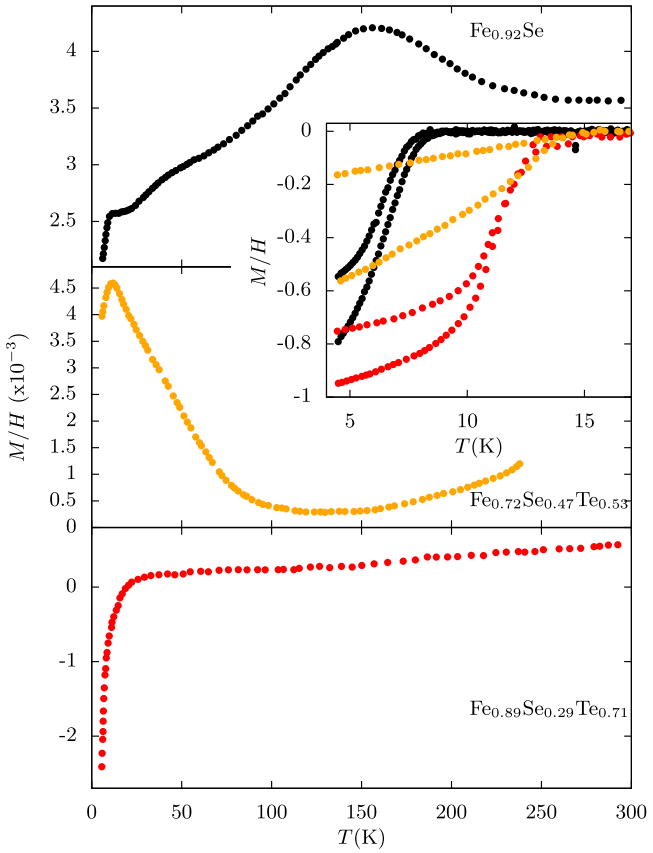

Figure 3. Temperature dependence of the magnetization for $Fe_{0.92}Se$, $Fe_{0.72}(Se_{0.47}Te_{0.53})$ and $Fe_{0.89}(Se_{0.29}Te_{0.71})$ crystals with a 0.1 T applied magnetic field perpendicular to the crystal plane. Inset: superconducting volume fraction, measured with $\mu_0 H = 0.2$ mT.

magnetic field of $\mu_0 H = 0.2$ mT perpendicular to the crystal plane. We obtain a superconducting volume fraction of 80%, 56% and 94% for $Fe_{0.92}Se$, $Fe_{0.72}(Se_{0.47}Te_{0.53})$ and $Fe_{0.89}(Se_{0.29}Te_{0.71})$, respectively.

3. Results and discussion

Figure 4(a) shows the typical behavior of the in plane resistivity as a function of temperature for crystals of $Fe_{1-y}(Se_{1-x}Te_x)$. As analyzed below, due to the coexistence of the tetragonal and hexagonal phases, and depending on the value of the resistivity, ρ, of each phase and on the domain size of each phase, ρ might present characteristics of both phases.

3.1. Normal state properties

The main features of the normal state resistivity in samples of the β-phase have been described in the literature [19–22]. A metallic-like behavior was reported for the Se rich end. The Te doping in samples with only β-phase presents a metallic behavior below a certain T^*. Excess Fe in these samples results in a weak localization regime. In the Te rich end, a marked magnetic and structural anomaly at $\simeq$70 K that separates two different resistivity behaviors was reported. In Fe deficient compounds, the resistivity is metallic-like in

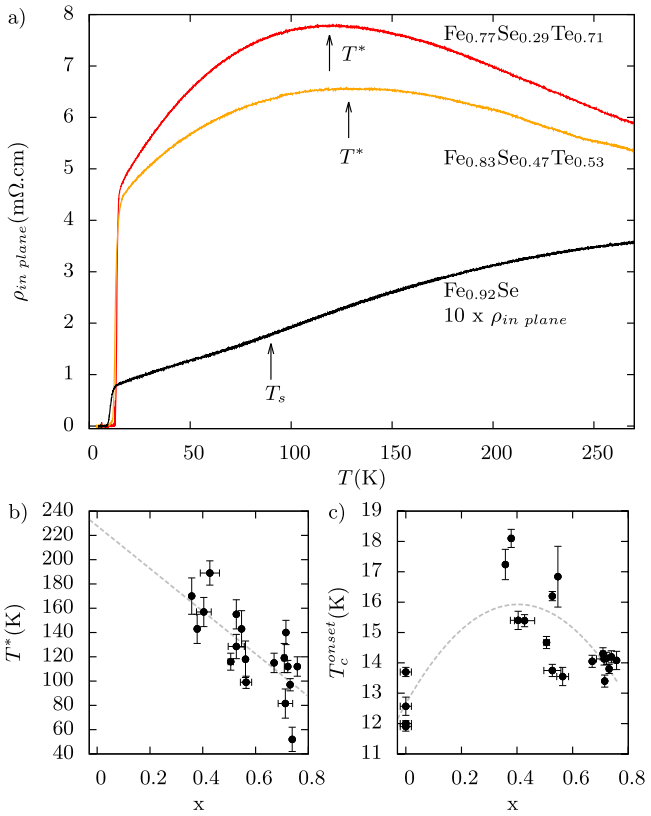

Figure 4. (a) Temperature dependence of the in-plane resistivity for $Fe_{0.92}Se$, $Fe_{0.83}(Se_{0.47}Te_{0.53})$ and $Fe_{0.77}(Se_{0.29}Te_{0.71})$ crystals. T_s indicates the temperature of the structural transition and T^*, the maximum in the resistivity. (b) T^* and (c) T_c^{onset} as a function of the Te content. The dotted lines are guides to the eye.

Fe_7Se_8 with an important drop at $T \simeq 60$ K which is related [23] to a magnetic reorientation at $T \sim 130$ K while Fe_2Te_3 presents a semiconducting behavior [24].

The in plane resistivity of our $Fe_{1-y}Se$ crystals exhibits a metallic-like behavior down from room temperature with a change in the slope at $T_s \simeq 90$ K. This change is associated with a structural transition of the β-phase from tetragonal to orthorhombic [25]. Our neutron diffraction experiments on powders (see appendix) clearly support this fact. In Te doped samples, the resistivity increases with decreasing temperature until a certain T^* at which it becomes metallic-like. This is a common feature of all of our samples, and increasing the Te content, T^* decreases as shown in figure 4(b). On the other hand, T^* has no dependence on the Fe content within the range studied in this work. Moreover, we have found no evidence of weak localization as reported in [21]. The behavior above T^* is unlikely to be related to the semiconducting hexagonal phase Fe_2Te_3 because it is also seen in pure β-phase crystals, both in the literature [20] and in our crystals. It does not have a clear and unique interpretation but it may be related with the maximum in resistivity of β-FeSe at 350 K [26]. Furthermore, the Te dependence of T^* has the same behavior as the pressure dependence of the resistivity maximum in $Fe(Se_{0.5}Te_{0.5})$ [27] where T^* increases with pressure. In our case, Te replacement by Se is equivalent to a positive pressure that is reflected in an increase of T^* with Se content.

3.2. Superconducting behavior

As we have stated in the previous section, the lower the amount of Fe the greater the proportion of hexagonal phase, but this varies with the Se content. This fact is also made evident in the superconducting transition. Our $Fe_{1-y}Se$ crystals present a transition around $T_c^{\text{onset}} \simeq 12$ K, higher than the transition temperature for pure β-phase samples ($T_c = 8.5$ K) [28]. As customary, the transition temperature is defined by the intersection of the linear extrapolation from the normal state and the transition zone.

The possibility of stress at the interfaces between the hexagonal and tetragonal phases and in consequence increment of the transition temperature is discussed in the appendix. In brief, a systematic widening of the neutron diffraction peaks for the samples with mixture of phases, corresponds to the existence of such stresses, that have an influence on the pressure dependent T_c. On the other hand, the Te dependence of the transition temperature presents a maximum at $x \simeq 0.4$ as is expected from other results in the literature [29], see figure 4(c).

We will now discuss the superconducting state of Fe deficient $Fe_{1-y}(Se_{1-x}Te_x)$ crystals analyzing the effect of the microscopic mixture of phases in the vortex state dissipation in transport experiments. Given the tetragonal layered crystalline structure these compounds are expected to present anisotropic electronic properties that will manifest also in the mixed state.

3.2.1. Intrinsic anisotropy ($H_{c2\parallel}/H_{c2\perp}$). Figure 5(a) shows the in plane transition for a $Fe_{0.99}(Se_{0.33}Te_{0.67})$ single crystal at various magnetic fields perpendicular to the crystal surface, $H_\perp$. Similar behavior is observed for other compositions. The transition is broadened by about 15% from 0 to 16 T. This broadening is consistent with a thermal activated behavior of the vortex lattice, see section 3.2.2.

The superconducting phase diagrams for fields parallel, $H_\parallel$, and perpendicular, $H_\perp$, to the platelet's plane are shown in figure 5(b). The definition of H_{c2} is given by the temperature of the onset of the transition for each applied field defined as the intersection between the linear extrapolations from normal and transition zones. The difference between both orientations makes evident that the material is slightly anisotropic. The ratio $\gamma_m = H_{c2\parallel}/H_{c2\perp}$ indicates that the anisotropy increases with temperature in agreement with other works [19, 30], see figure 5(c). For $Fe_{1-y}Se$, the anisotropy between in plane and out of plane H_{c2} measurements also increases with temperature, with γ_m being approximately 1.2. However, as discussed in previous sections, the superconducting β-phase has two main orientations perpendicular to the planar surface of the samples (i.e. 00l and l0l), therefore making the measured value of γ_m lower than the value for the clean β-phase, found to be approximately 3 [38].

Using the conventional one-band WHH theory [30],

$$H_{c2}(0) = -0.693 \left.\frac{dH_{c2}}{dT}\right|_{T_c} T_c, \qquad (1)$$

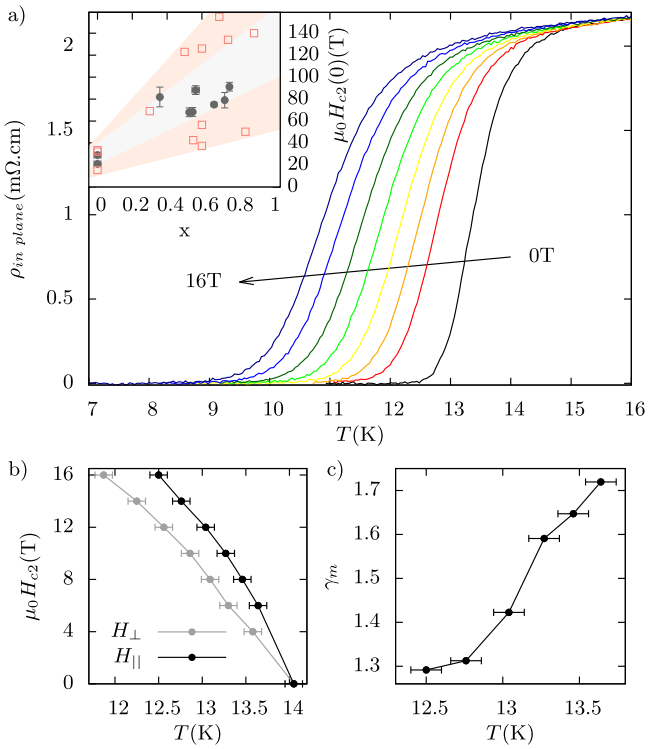

Figure 5. (a) Temperature dependence of the in plane resistivity for a $Fe_{0.99}(Se_{0.33}Te_{0.67})$ single crystal with $\mu_0 H_\perp$(0, 4, 6, 8, 10, 12, 14 and 16 T). The arrow show the direction of field increase. Inset: Te composition dependence of $H_{c2\perp}(0)$ for our data (gray circles) and values extracted from the literature [30–37]. (b) Phase diagram for $H_{c2\parallel}$ and $H_{c2\perp}$. (c) Temperature dependence of the anisotropy γ_m.

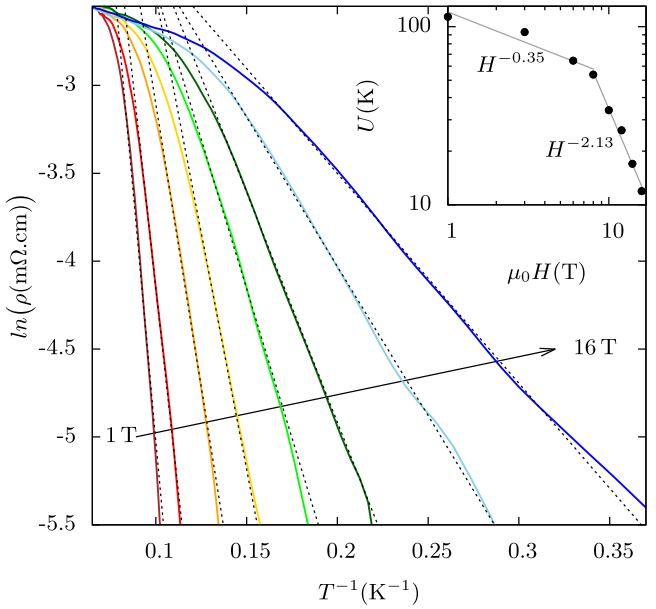

Figure 6. Logarithm of the in plane resistivity as a function of T^{-1} for $Fe_{0.91}Se$. The dotted lines are the fit of equation (2) for each magnetic field ($\mu_0 H$ = 1, 3, 6, 8, 10, 12, 14, 16 T). Inset: activation energy for the vortex movement as a function of the applied magnetic field. The solid line is the fit of $U_0 H^{-q}$.

we obtained the value of $H_{c2\perp}(0)$ as a function of composition. The inset of figure 5 shows the comparison of our data with those extracted from the literature [30–37]. As reported by other authors for samples with Fe excess [37], in our Fe deficient samples it can be observed that also $H_{c2}(0)$ increases with the content of Te.

3.2.2. Broadening of $\rho(T)$-activated behavior. Figure 6 shows the logarithm of the resistivity versus T^{-1}, for several applied magnetic fields perpendicular to the crystal surface. The linear behavior over a wide temperature range suggests that a thermally activated flux motion model [39] suitably encodes the broadening of the transition in $Fe_{0.91}Se$. Thus, in order to describe the dissipation below H_{c2} in the region where the macroscopic critical current goes to zero, $J_c \to 0$, we used such an activated flux motion model [39].

In the linear response regime, the resistivity is well approximated by,

$$\rho = \rho_0 \exp\left(\frac{-U(H,T)}{T}\right), \tag{2}$$

with the activation energy

$$U(H,T) = U_0 H^{-q}\left(1 - \frac{T}{T_c}\right). \tag{3}$$

Here, T is the temperature, H is the applied magnetic field, U_0, ρ_0 and q are constants and T_c is the transition temperature at $\mu_0 H = 0$ T. Figure 6 also shows the fits to the data. The activation energy extracted from the slope of these fits is shown on the inset. The two values of the q exponent for the lowest and highest fields are found in several works [31, 35, 40] but they do not have a clear interpretation.

3.2.3. Angular dependence $\rho(\theta)$ in $Fe_{1-y}(Se_{1-x}Te_x)$. The interpretation of the results in the previous paragraphs (sections 3.2.1 and 3.2.2) requires to consider the following framework: the dissipative regime observed in our samples may be related both to the electronic anisotropy of the material and to the nature of the defects in the structure. Close to the normal state, the resistivity is concomitant to intrinsic superconducting properties (higher critical field, mass anisotropy). Below a certain ρ/ρ_n value, that depends on the nature of the defects [41], the dissipation is affected by an effective viscosity that hinders the movement of vortices, thereby affecting the activated behavior. Hence, by means of the activated movement picture, one may obtain an effective activation energy that gives information on the nature of the defects as pinning centers.

Thus, in order to study the influence of possible correlated defects, we measured the angular dependence of the dissipation in transport experiments below the onset of the superconducting state. We used a constant Lorentz force configuration, maintaining the measuring current along the rotation axis of the crystal. The perpendicular to the crystal's surface is 0° in our notation.

Figure 7 shows the angular dependence of the in plane resistivity, $\rho_{\text{in plane}}$, for $Fe_{0.91}Se$, $Fe_{0.8}(Se_{0.45}Te_{0.55})$ and $Fe_{0.99}(Se_{0.33}Te_{0.67})$ for $\mu_0 H = 12$ T and $T = 6.70(2)$ K, $T = 13.00(7)$ K and $T = 11.80(7)$ K, respectively. For each sample, the temperature is chosen so that $\rho(T)/\rho(T_c) \sim 0.5$.

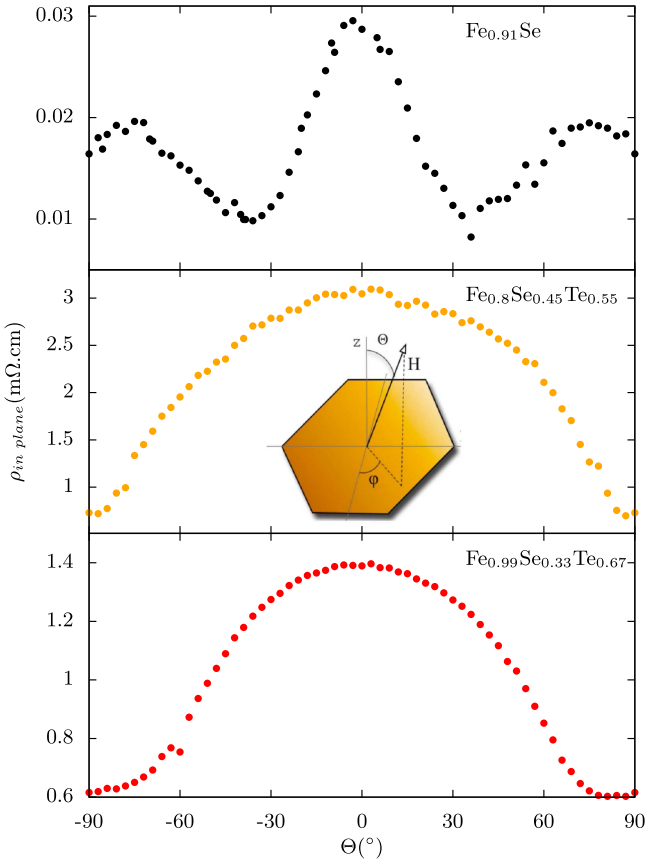

Figure 7. Angular dependence of the in-plane resistivity for $Fe_{0.91}Se$, $Fe_{0.8}(Se_{0.45}Te_{0.55})$ and $Fe_{0.99}(Se_{0.33}Te_{0.67})$ single crystals with $\mu_0 H = 12$ T and $T = 6.70(3)$ K, $T = 13.00(7)$ K and $T = 11.80(7)$ K, respectively. The inset is a sketch of the sample with the Θ angle definition. The in plane applied current is always perpendicular to the field.

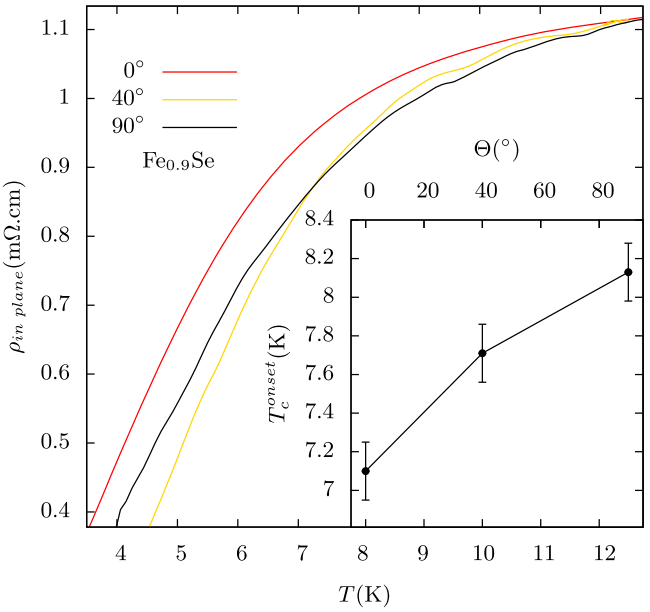

Figure 8. Temperature dependence of the resistivity of $Fe_{0.9}Se$ with $\mu_0 H = 14$ T for three different angles ($\Theta = 0°$, 40° and 90°). Inset: critical temperature as a function of the angle, Θ.

According to the model [42] of an anisotropic material with point defects, the resistivity, at a fixed H and T, should have a maximum at 0°, a minimum at 90° and behave monotonically between these two extremes. To be specific, the angular dependence [42] should be given by, $\rho(\Theta, H, T) = \rho(H\varepsilon_\Theta, T)$, where $\varepsilon_\Theta^2 = \cos^2\Theta + \gamma^{-2}\sin^2\Theta$ and γ is the mass anisotropy of the material. In our case, crystals with Te display this behavior but with small discrepancies in the slope of the curves approaching the orientation of 90°. Such discrepancies do not relate to the Te or Fe concentration. On the other hand, $Fe_{1-y}Se$ presents two deep minima at $\Theta \sim \pm 34°$. These extra minima were found in all the samples in a wide range of fields and temperatures below T_c^{onset}. Furthermore, for the larger crystals, these 34° minima appear independently of the direction of the current in the crystal plane and on the contact arrangement (not shown here). In the literature, similar measurements of angular dependence for FeSe [43] have been reported.

In principle, one could relate the anomalous behavior of the dissipation in $Fe_{1-y}Se$ either to intrinsic properties of the material or to the microstructure related vortex dynamics. However, as confirmed by our measurements, H_{c2} and T_c^{onset} are intrinsic characteristics of the material that vary monotonously with the angle between 0° and 90° and only depend on the anisotropy of the material [42]. Also, it should be mentioned that the multiband nature of the electronic properties of β-FeSe does not affect the angular dependence of $H_{c2}(T, \Theta)$ and $T_c^{\text{onset}}(H, \Theta)$ [38]. Related to the above, figure 8 shows the temperature dependence of the resistivity for $Fe_{0.9}Se$ with $\mu_0 H = 14$ T at $\Theta = 0°$, $\Theta = 40°$ and $\Theta = 90°$. The critical temperature has a monotonic behavior with angle, see inset of figure 8. Then as T_c^{onset} and H_{c2} have the same dependence in Θ, we can conclude that the anomalous behavior of the resistivity is governed by vortex dynamics. Furthermore, the curve at $\Theta = 40°$ crosses the curve at $\Theta = 90°$ and the difference increases with decreasing temperature. This is another indication that it is related to vortex movement. The presence of correlated defects has more influence in the resistivity as the temperature decreases due to the reduction of vortex mobility.

As presented in the previous section, the dissipation is well described by an Arrhenius law. Figure 9 presents the angular dependence of the activation energy for $Fe_{0.91}Se$. The data exhibit two contributions to the activation energy. One comes from point defects and is represented by the solid line. The other at $\Theta \sim \pm 34°$ comes from a possible structure of correlated defects which act as pinning centers. To understand this contribution and the difference with Te doped samples, we focus on the crystal structure of our samples.

3.2.4. Microstructural angular investigation. In the XR diffraction patterns we identified the $Fe_{1-y}Se$ (00l) and (l0l) families and the (00l) one for the Fe_7Se_8 spurious phase, see figure 1. This mixture of phases and the interfaces between them could be the microscopic origin of the correlated defects

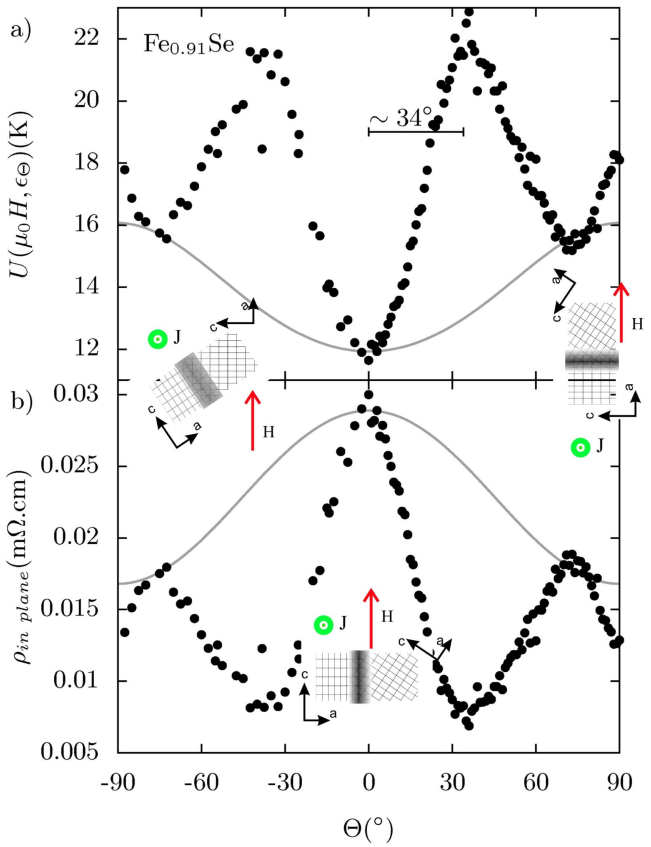

Figure 9. (a) Angular dependence of the activation energy and (b) angular dependence of the in plane resistivity, both for a single crystal of $Fe_{0.91}Se$ for $\mu_0 H = 16$ T and $T = 4.90(3)$ K. The solid line represents the expected behavior for an anisotropic material, with $\gamma = 1.20(5)$, in the presence of only point defects. The sketches represent the *a* and *c* axis direction with respect to the current and applied field.

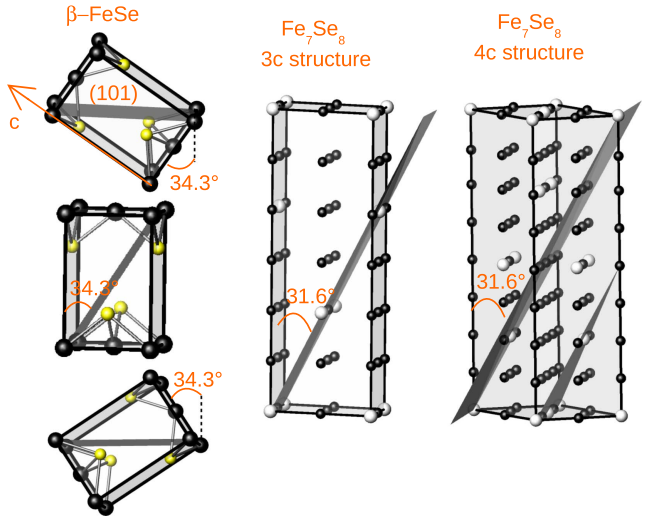

Figure 10. Drawing of the crystal structure of our samples. Unit cell of the tetragonal phase (left) with the different orientations of the *c* axis and the unit cell of the hexagonal phase (right) for the two possible superstructures 3*c* and 4*c*. For the hexagonal phase we only show the Fe atoms in black and the vacancies in white.

acting as pinning center in $Fe_{0.91}Se$. As we already said, there is a nanoscale intergrowth of both phases and its shape and size depends on the crystal growth parameters [6]. In the hexagonal phase, the vacancies are ordered as a superstructure. Due to the crystal growth procedure, the most likely superstructure is the one called 3*c*, in which the lattice parameter of the superstructure is three times that of the normal cell [44]. But the 4*c* structure could also be present, as we show from neutron diffraction data in the appendix. In either case there is a dense plane of vacancies at an angle ∼32° of the *c* axis, i.e. the plane (*l*0*l*). On the other hand, the tetragonal phase has twofold orientation of the *ab* plane. One is parallel to the crystal surface and the other is at ±34(1)° to the normal of the surface, considering the measured lattice parameters $a = 0.379(1)$ nm and $c = 0.552(1)$ nm. Unit cells for the different phases of ours crystals are shown in figure 10. Therefore, the *ab* plane of the tetragonal phase is close to the most dense plane of vacancies of the 3*c* or 4*c* structure of the hexagonal Fe_7Se_8 phase. This could be acting as seed for both *β*-phase orientations during growth and it is a possible correlated defect. Additionally, when the magnetic field is applied in the direction $\Theta = \pm 34(1)°$, the vortices are crossing the *ab* plane in their movement. Using the angular dependence of the dissipation described above, we know that the resistivity has a minimum when the vortices cross the *ab* plane.

In figure 11(a) we show an XR diffraction pattern, fixing the diffraction condition at $\chi = 55.62°$, $\phi = 43.7°$. The sketch in the inset of figure 11(b) shows the χ and ϕ angles geometry. In this condition we see that the *ab* plane and the (101) peak of the tetragonal phase are parallel to the (101) peak of the hexagonal phase. This is consistent with the dense plane of vacancies being the interface with the tetragonal phase in spite of the mismatch of 2° between the planes of both phases.

Microscopically, this boundary matching both phases should have just one direction and the minima in the dissipation as a function of the angle Θ should not be symmetric with respect to the $\Theta = 0°$ direction. We have found this situation only in very small samples with a platelet surface of 2500 μm^2 or less. For larger samples, as that shown in figure 11(b), the pinning structure is symmetric and we have found the resistance minima at $\Theta = \pm 34(1)°$ for different directions of the current and contact arrangements as long as a constant Lorentz force is maintained. These large samples have a characteristic platelet surface topography, namely that observed in figure 11(b) that shows lines with a six-fold symmetry. To understand the boundary on the plane of the crystal and the two symmetrical minima on the angular dependence of the resistivity we include, in figure 11(b), ϕ angle scans at three χ angles. The pattern corresponding to $\chi = 0$ and the (101) diffraction shows the background. From the measured patterns in a ϕ scan we observed the (001) and the (200) diffractions, of the tetragonal *β*-phase, corresponding to the *c*-axis and *a*-axis directions respectively displaying a sixfold geometry. Therefore, the intergrowth of the hexagonal phase is modifying the rotational symmetry of the tetragonal phase.

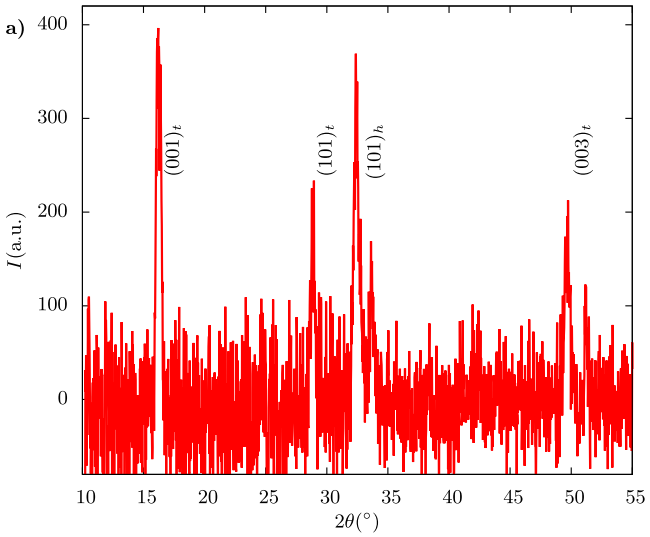

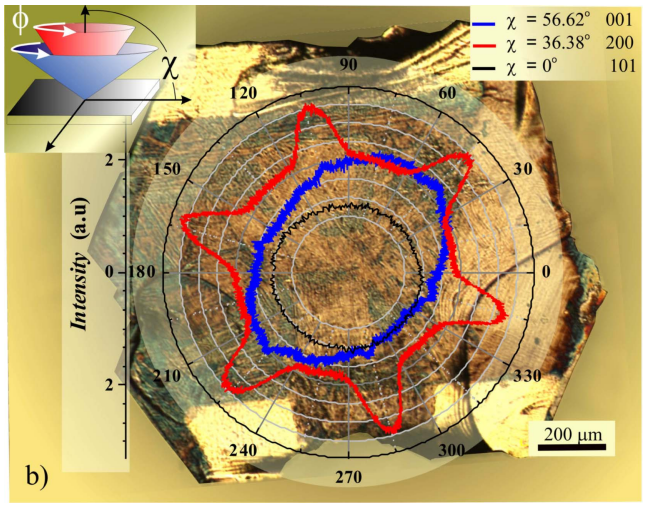

Figure 11. (a) XR diffraction pattern taken at $\chi = 55.62^\circ$ and $\phi = 43.7^\circ$. The Miller indices of tetragonal phase and the hexagonal phase are indicated. (b) Polar graphs of the XR diffraction ϕ scans patterns for the sample in (a) taken at different values of the azimuthal angle χ coincident with the (001), (200) and (101) reflexions of the β phase indicated with blue, red and black lines superimposed to the sample photograph. The sketch in the upper inset indicates the geometry of χ and ϕ angles.

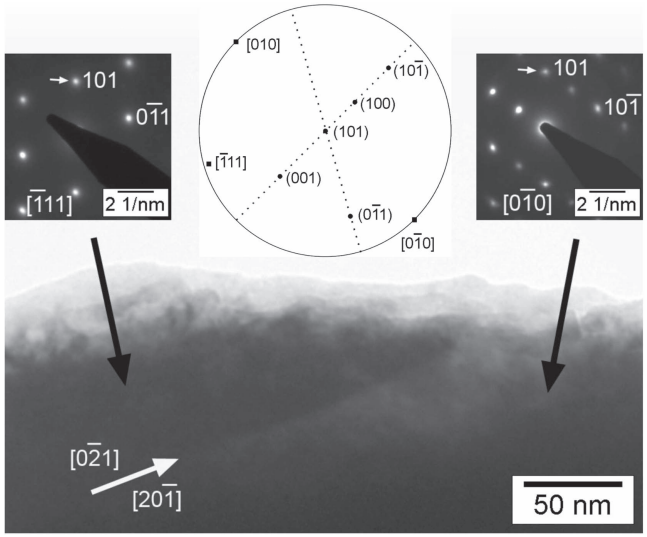

Figure 12. Transmission electron microscopy image of an $Fe_{0.9}Se$ crystal from a cross-section view. The diffraction patterns corresponding to the two observed orientations of the beta-phase have in common the 101 spot. The sketch indicates the stereographic projection of the tetragonal structure centered on the normal of the (101) plane.

For further assessment, TEM images were taken from cross-section samples. In figure 12 the bright field image including an interface between two orientations of the tetragonal β-phase can be observed. The corresponding selected area electron diffraction patterns show that the $\langle 111 \rangle$-type zone axis of the crystal on the left side is parallel to the $\langle 010 \rangle$-type zone axis of the crystal on the right side, having in common the 101 spot indicated by an arrow. The correspondence between the two crystals can be rationalized from the stereogram, sketched in the figure, centered on the normal of the crystal surface, and oriented to match one of the six-fold geometry orientations of the tetragonal structure shown in figure 11(b). It can be observed that there are 120° between $[0\bar{1}0]$ and $[\bar{1}11]$ directions corresponding to the zone axis diffraction patterns observed in figure 12. Therefore, the two orientations observed by TEM are in accordance to the many-fold orientations observed by XR diffraction. The trace of the interface is close to the $\langle 201 \rangle$-type direction in both tetragonal structures and is indicated by a white thick arrow in figure 12. Although the presence of the hexagonal phase was not observed at the interface of these two tetragonal domains, the angle between them is consistent with six-fold symmetry depicted in large samples as that of figure 11(b).

As a final remark, we want to go back to the very different scenario observed in the angular dependence of the resistivity on the samples with Te in figure 7. The absence of the extra resistivity minimum at $\Theta = \pm 34(1)^\circ$ indicates that there are no correlated defect in this case. As seen in figure 3, the magnetic order, that is related with the vacancy order, is rapidly diluted with the inclusion of Te. Now there is no dense plane of vacancies in the hexagonal phase and therefore there is not a clear interface between the two phases. As a consequence, the angular dependences of the resistivity are similar only to those of point defects.

4. Conclusion

We have presented the angular dependence of dissipation in the superconducting state of FeSe and $Fe(Se_{1-x}Te_x)$ using crystalline materials with $Fe_{1-y}(Se_{1-x}Te_x)$ intergrowth. This intergrown material is a solid solution from $Fe_{0.875}Se$ to $Fe_{0.667}Te$. We found that correlated defects are revealed as a hallmark of the angular dependence, in particular near the Se reach end. The in plane resistance in the superconducting state as well as the activation energy of the thermally activated response are consistent with the presence of correlated defects. These correlated defects act as pinning centers for the vortices in very well defined angles, ±34° from the crystal's normal, in the case of $Fe_{1-y}Se$. By adding Te, these defects

disappear and there is not a clear indication of them in the angular dependence of the in plane resistance. We have presented an analysis of the microscopic nature of these defects based in the structure of the intergrown materials, which are the superconducting β-Fe($Se_{1-x}Te_x$) and the iron deficient hexagonal phase $Fe_{1-y}(Se_{1-x}Te_x)$. The latter Fe deficient phase is magnetic near the Se reach end and was found to be a hexagonal material with two set of vacancies arrangements as related to the observed magnetic bulk properties as well as in the neutron diffraction experiments. The existence of intergrowth of this phase favored the presence of two main orientations of β-Fe($Se_{1-x}Te_x$) in the crystals, and apparently plays a key role for the origin of the correlated defects structure. The matching of both atomic structures define the growth habit of the crystalline material as well as the correlated defects orientation.

Furthermore, information on intrinsic superconducting properties was provided. We reported an increase of the critical superconducting field with the Te content and a maximum in the critical temperature for Te content $x \simeq 0.4$. An increase in T_c was observed with respect to crystals with only the β phase, which may be related with tensions on the interphase between the tetragonal and the hexagonal phases. For the resistivity in the normal state, we reported a maximum at a temperature that increases with Se content.

Acknowledgments

We thank F Gennari for help in sample preparation. Work partially suported by Conicet PIP 2014-0164, ANPCyT, PICT 2014-1265 and Sectyp U N Cuyo. Funding of this research by Spanish MINECO and FEDER programme (Project ENE2014-52105-R-9) is gratefully acknowledged by AB-M. JC acknowledges the Grant No. MAT2015-68200-C2-2-P from the Spanish MINECO. Neutron diffraction experiments conducted at the LLB, were supported through the research proposals 11844, 12353 and 12354.

Appendix

Neutron diffraction analysis of $Fe_{1-y}Se$ polycrystalline material

Neutron powder diffraction was used to characterize the vacancy superstructure of the hexagonal phase Fe_7Se_8 and to investigate possible strain effects due to the mixture of phases. We performed the neutron powder diffraction experiment at the Laboratoire León Brillouin in the G4.1 instrument with $\lambda = 0.2426$ nm. We also measured at the high resolution instrument 3T2 with $\lambda = 0.1960$ nm to study the structural transition of the tetragonal phase. We compared two synthesized polycrystalline samples of FeSe, one with pure β-phase, and the other with a mixture of tetragonal and hexagonal phases in a similar percentage as the crystals studied in this work.

The polycrystals were obtained as described in section 2 using a maximum temperature of 680 °C for 48 h and of 437 °C for 1 month for the samples with mixture of phases and with pure β-phase respectively. The analysis of the neutron diffraction pattern revealed the mixture of tetragonal and hexagonal phases in the first case that we will refer as $Fe_{1-y}Se$ and the presence of only the tetragonal phase β-FeSe in the other, see inset of figure A1.

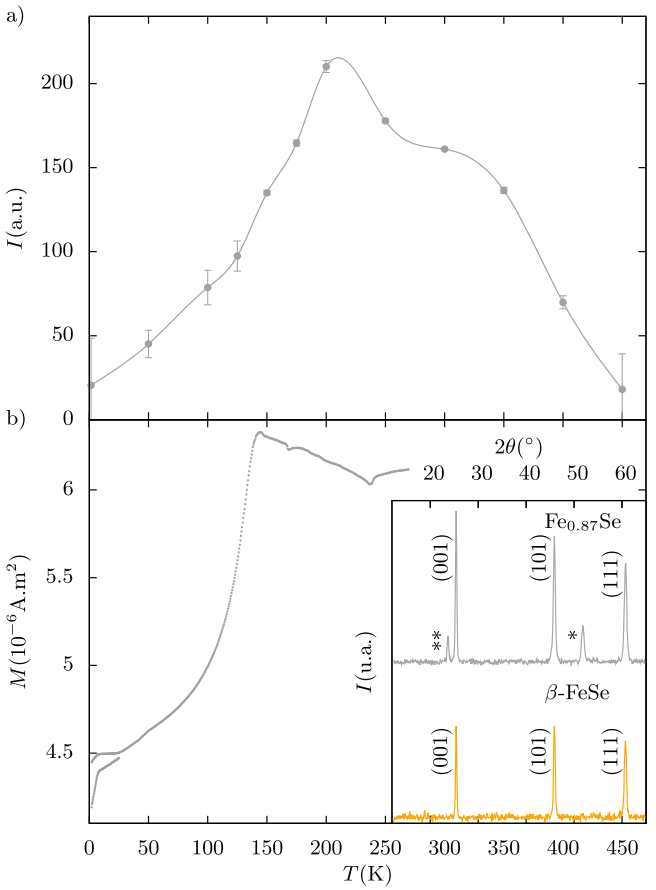

Figure A1. (a) Temperature dependence of the integrated intensity of the magnetic reflection (001) in the 2θ range 21.7°–24.3° for $Fe_{1-y}Se$, the line is a guide to the eye. (b) Magnetization for $Fe_{1-y}Se$ with an applied magnetic field of 20 Oe. Inset: neutron diffraction patterns for $Fe_{1-y}Se$ and β-FeSe for $T = 250$ K. The tetragonal phase Miller indices are indicated in brackets. $*$ indicates peaks corresponding to the hexagonal phase and $**$ indicates the magnetic peak (001) of the hexagonal structure.

Figure A1(a) shows the integrated intensity of the magnetic reflection (001), marked with $**$ in the inset, as a function of the temperature. This gives information about the vacancy order superstructure, present in $Fe_{1-y}Se$. In the pure $4c$ superstructure, a gradual drop below 210 K has been reported [18] for the (001) magnetic reflection. Nevertheless, for the $3c$ superstructure, the same magnetic reflection shows a sudden drop, indicative of a spin reorientation around 140 K (recall that magnetic peaks relate to the projection of the magnetic moment on the plane perpendicular to the given direction). In agreement with the above, the behavior observed in figure A1(a) indicates a mixture of the $3c$ and $4c$ phases. The behavior of the bulk magnetization, shown in figure A1(b), displays a steep increment with increasing temperature, with a maximum at 140 K. This trend may be

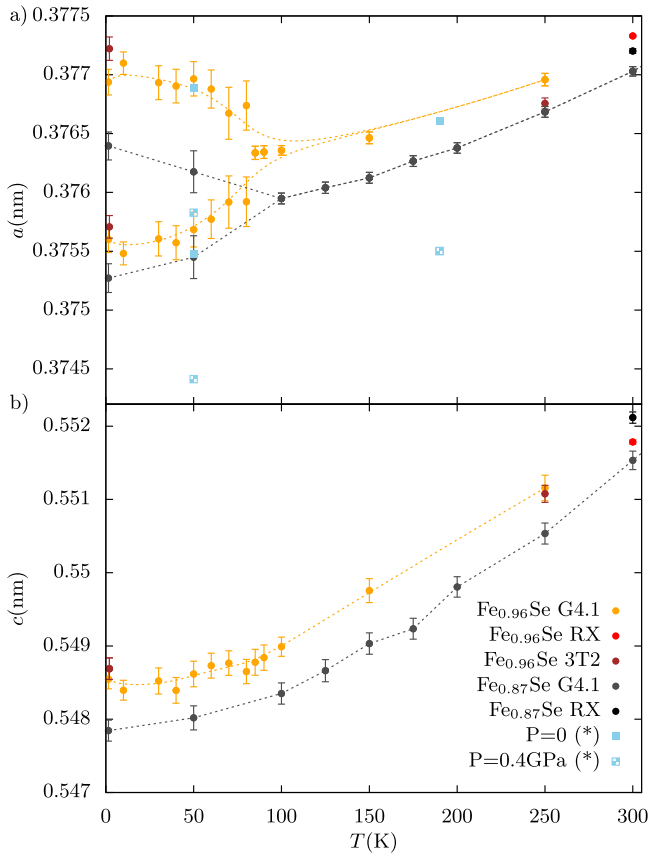

Figure A2. (a) Temperature dependence of the lattice parameter a in the tetragonal phase and $a/\sqrt{2}$ and $b/\sqrt{2}$ in the orthorhombic phase and (b) of the c axis parameter for β-FeSe and $Fe_{1-y}Se$. The symbols correspond to XR or neutron diffraction data as indicated, also data marked with $*$, taken from [45] with and without applied pressure are plotted for comparison.

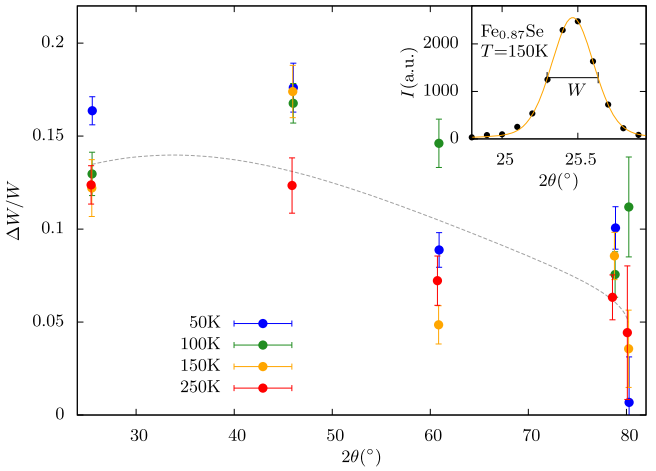

Figure A3. Normalized difference peak width, $\frac{\Delta W}{W} = \frac{2(W(Fe_{1-y}Se) - W(\beta\text{-FeSe}))}{W(Fe_{1-y}Se) + W(\beta\text{-FeSe})}$ for the different reflections and temperatures. Inset: example of the fit of the Pseudo-Voigt function for the (001) reflection for $Fe_{1-y}Se$ at $T = 150$ K.

reconciled with the neutron diffraction analysis also in terms of the coexistent $3c$ and $4c$ superstructures. The magnetic subnetwork related to the $4c$ structure smoothly starts reorientation towards the (001) direction when the temperature decreases below 210 K, getting closer to the easy axis of the $3c$ structure. The neutron diffraction intensity diminishes, but the bulk magnetization increases. On the other side, the $3c$ subnetwork undergoes a sudden reorientation at around 140 K, and at this point the bulk magnetization quickly falls with decreasing temperature. This is consistent with a mixture of $3c$ and $4c$ superstructures [17]. The magnetization of the crystalline samples, figure 3(a) in section 2 shows that it probably has the same mixture of superstructures.

From the analysis of the neutron diffraction data, we also obtained the temperature dependence of the lattice parameters of the β-phase for the two polycrystals under study, see figure A2. In both cases, there is a structural transition at ∼90 K from tetragonal P4/nmm to orthorhombic Cmma. There is a good agreement between the lattice parameters obtained with neutron diffraction at the G4.1 instrument, the 3T2 instrument and with XR measurements. On the other hand, there is a small difference between the lattice parameters obtained from the β-FeSe and the sample with mixture of phases.

This difference is not enough to explain the increment of transition temperature in the resistivity described in section 3.2. Given the sensitivity to external pressure, it was reported that a change in T_c of ∼3.5 K is obtained with a pressure of 0.4 GPa [46]. The difference of the lattice parameter a obtained in [45] at 0 and 0.4 GPa is larger than the difference obtained for the two samples under study, as shown in figure A2. A systematic microstructural observation accompanies the variation in the critical temperature in our resistivity data. In this case, broader peaks in the diffraction pattern of the sample with mixture of phases are expected. To confirm this, we fitted a Pseudo-Voigt function to each peak of the tetragonal phase with the lorentzian and gaussian weight defined by the Rietveld refinement of the whole diffractogram at that temperature. Figure A3 shows the ratio between the difference and the average of the measured tetragonal peak width in $Fe_{1-y}Se$ and β-FeSe. For all temperatures and reflections, the polycrystal with mixture of phases presented wider peaks. This could be interpreted in terms of tensions in the sample with mixture of phases (probably at the boundary regions), defective structures, grain size disorder, etc.

References

[1] Kasahara S *et al* 2016 *Nat. Commun.* **7** 12843
[2] Sun J *et al* 2016 *Nat. Commun.* **7** 12146
[3] Mizuguchi Y and Takano Y 2010 *J. Phys. Soc. Japan* **79** 102001
[4] Schuster W, Mikler H and Komarek K L 1979 *Mon. Chem./ Chem. Mon.* **110** 1153–70
[5] Chareev D, Osadchii E, Kuzmicheva T, Lin J Y, Kuzmichev S, Volkova O and Vasiliev A 2013 *CrystEngComm* **15** 1989–93
[6] Wittlin A, Aleshkevych P, Przybylińska H, Gawryluk D J, Dłużewski P, Berkowski M, Puźniaka R, Gutowsk M U and Wiśniewski A 2012 *Supercond. Sci. Technol.* **25** 065019
[7] Gawryluk D J, Fink-Finowicki J, Wiśniewski A, Puźniak R, Domukhovski V, Diduszko R, Kozłowski M and Berkowski M 2011 *Supercond. Sci. Technol.* **24** 065011

[8] Sales B C, Sefat A S, McGuire M A, Jin R Y, Mandrus D and Mozharivskyj Y 2009 *Phys. Rev.* B **79** 094521
[9] Argyriou D N *et al* 2010 *Phys. Rev.* B **81** 220503
[10] Gresty N C *et al* 2009 *J. Am. Chem. Soc.* **131** 16944–52
[11] Fang M H, Pham H M, Qian B, Liu T J, Vehstedt E K, Liu Y, Spinu L and Mao Z Q 2008 *Phys. Rev.* B **78** 224503
[12] Grønvold F, Haraldsen H and Vihovde J 1954 *Acta Chem. Scand.* **8** 1927
[13] Okazaki A and Hirakawa K 1956 *J. Phys. Soc. Japan* **11** 930–6
[14] Zhang S B *et al* 2009 *Supercond. Sci. Technol.* **22** 015020
[15] Terzieff P 1981 *Physica* B+C **103** 158–64
[16] Yeh K, Ke C, Huang T, Chen T, Huang Y, Wu P and Wu M 2009 *Crystal Growth Des.* **9** 4847–51
[17] Terzieff P and Komarek K L 1978 *Mon. Chem./Chem. Mon.* **109** 1037–47
[18] Kawaminami M and Okazaki A 1970 *J. Phys. Soc. Japan* **29** 649–55
[19] Fang M, Yang J, Balakirev F F, Kohama Y, Singleton J, Qian B, Mao Z Q, Wang H and Yuan H Q 2010 *Phys. Rev.* B **81** 020509
[20] Sudesh, Rani S, Das S, Rawat R, Bernhard C and Varma G D 2012 *J. Appl. Phys.* **111** 07E119
[21] Liu T J *et al* 2009 *Phys. Rev.* B **80** 174509
[22] McQueen T M *et al* 2009 *Phys. Rev.* B **79** 014522
[23] Kawaminami M and Okazaki A 1967 *J. Phys. Soc. Japan* **22** 925
[24] Aramu F and Manca P 1964 *Il Nuovo Cimento* **33** 1025–30
[25] McQueen T M, Williams A J, Stephens P W, Tao J, Zhu Y, Ksenofontov V, Casper F, Felser C and Cava R J 2009 *Phys. Rev. Lett.* **103** 057002
[26] Karlsson S, Strobel P, Sulpice A, Marcenat C, Legendre M, Gay F, Pairis S, Leynaud O and Toulemonde P 2015 *Supercond. Sci. Technol.* **28** 105009
[27] Horigane K, Takeshita N, Lee C H, Hiraka H and Yamada K 2009 *J. Phys. Soc. Japan* **78** 063705
[28] Amigó M L, Crivillero V A, Franco D G and Nieva G 2014 *J. Phys.: Conf. Ser.* **568** 022005
[29] Katayama N *et al* 2010 *J. Phys. Soc. Japan* **79** 113702
[30] Lei H, Hu R, Choi E S, Warren J B and Petrovic C 2010 *Phys. Rev.* B **81** 094518
[31] Ge J, Cao S, Shen S, Yuan S, Kang B and Zhang J 2010 *Solid State Commun.* **150** 1641–5
[32] Kida T, Kotani M, Mizuguchi Y, Takano Y and Hagiwara M 2010 *J. Phys. Soc. Japan* **79** 074706
[33] Kida T, Matsunaga T, Hagiwara M, Mizuguchi Y, Takano Y and Kindo K 2009 *J. Phys. Soc. Japan* **78** 113701
[34] Khim S, Kim J W, Choi E S, Bang Y, Nohara M, Takagi H and Kim K H 2010 *Phys. Rev.* B **81** 184511
[35] Yadav C S and Paulose P L 2009 *New J. Phys.* **11** 103046
[36] Lei H *et al* 2012 *Phys. Rev.* B **85** 094515
[37] Yeh K W, Hsu H C, Huang T W, Wu P M, Huang Y L, Chen T K, Luo J Y and Wu M K 2008 *J. Phys. Soc. Japan* **77SC** 19–22
[38] Amigó M L, Ale Crivillero M V, Franco D G, Guimpel J and Nieva G 2015 *J. Low Temp. Phys.* **179** 15–20
[39] Palstra T T M, Batlogg B, van Dover R B, Schneemeyer L F and Waszczak J V 1990 *Phys. Rev.* B **41** 6621–32
[40] Palstra T T M, Batlogg B, Schneemeyer L F and Waszczak J V 1988 *Phys. Rev. Lett.* **61** 1662–5
[41] Figueras J, Puig T and Obradors X 2003 *Phys. Rev.* B **67** 014503
[42] Blatter G, Feigel'man M V, Geshkenbein V B, Larkin A I and Vinokur V M 1994 *Rev. Mod. Phys.* **66** 1125–388
[43] Patel U, Hua J, Yu S H, Avci S, Xiao Z L, Claus H, Schlueter J, Vlasko-Vlasov V V, Welp U and Kwok W K 2009 *Appl. Phys. Lett.* **94** 082508
[44] Okazaki A 1959 *J. Phys. Soc. Japan* **14** 112–3
[45] Millican J N, Phelan D, Thomas E L, Leão J B and Carpenter E 2009 *Solid State Commun.* **149** 707–10
[46] Bendele M, Ichsanow A, Pashkevich Y, Keller L, Strässle T, Gusev A, Pomjakushina E, Conder K, Khasanov R and Keller H 2012 *Phys. Rev.* B **85** 064517